Available online at www.sciencedirect.com
SCIENCE DIRECT
International Journal of Heat and Mass Transfer 49 (2006) 3429–3438
International Journal of HEAT and MASS TRANSFER
www.elsevier.com/locate/ijhmt

Solute segregation during modified vertical gradient freezing of alloyed compound semiconductor crystals with magnetic and electric fields

X. Wang [a], N. Ma [a,*], D.F. Bliss [b], G.W. Iseler [b]

[a] Department of Mechanical and Aerospace Engineering, North Carolina State University, Campus Box 7910, Raleigh, NC 27695, USA
[b] US Air Force Research Laboratory, Sensors Directorate, AFRL/SNHC, 80 Scott Road, Hanscom AFB, MA 01731, USA

Received 22 April 2005; received in revised form 11 March 2006
Available online 11 May 2006

Abstract

Single crystals of gallium–aluminum–antimonide are solidified from a solution of molten gallium–antimonide and aluminum–antimonide. Electromagnetic stirring can be induced in the melt by applying a weak electric field together with a weak axial magnetic field. This paper presents a numerical model which uses a Chebyshev spectral collocation method with a second-order implicit time integration scheme with Gauss–Lobatto collocation points. This investigation models the unsteady motion and solute transport during vertical gradient freezing by submerged heater growth with electromagnetic stirring. The radial homogeneity in the crystal improves as the solute's concentration increases.

1. Introduction

Single crystals of alloyed compound semiconductors such as gallium–aluminum–antimonide (GaAlSb) are extremely important materials because they serve as the basis of devices for long wavelength infrared (LWIR) and very long wavelength infrared (VLWIR) space-based imaging applications and are strong candidates for hyperspectral imaging applications. In addition, alloyed GaAlSb crystals with wider bandgaps and higher electrical resistivity for large circuits of terahertz devices must have compositional uniformity. Gallium–aluminum–antimonide crystals can be grown from a solution or melt by the liquid-encapsulated Czochralski (LEC) process or by the vertical gradient freeze (VGF) process. The LEC process is a top-seeded growth method which has distinct advantages because the crystal is viewed directly during growth and because there is no container in contact with the crystal. However, short-range compositional uniformity can be problematic due to buoyancy-driven convection in the melt, which randomly changes the composition of the melt in the boundary layer at the growth interface [1]. In addition, long-range crystal composition generally changes due to a changing melt composition for alloys with segregation coefficients not equal to unity [2]. Relatively good long-range compositional uniformity was achieved for a non-stoichiometric Sb-rich melt by the LEC process by Ohmori et al. [3]. However, only 25% of the melt volume was solidified because the continual increase of antimony in the melt as crystal growth progressed eventually caused the crystal–melt interface to breakdown due to constitutional supercooling. In the early-90s, Ostrogorsky [4] introduced a modification of the bottom-seeded VGF process in which a submerged heater separates the melt into two zones, namely, a lower melt and an upper melt. As crystal growth progresses, the crystal solidifies while the submerged heater is slowly raised in order to maintain a constant lower melt depth. The crystal is solidified from a solution of molten gallium–antimonide (GaSb) and aluminum–antimonide (AlSb). Unfortunately, there can be severe long-range axial segregation in the crystal if the process does not have a way to replenish the lower

* Corresponding author. Tel.: +1 919 515 5231; fax: +1 919 515 7968.
E-mail address: nancy_ma@ncsu.edu (N. Ma).

0017-9310/$ - see front matter © 2006 Elsevier Ltd. All rights reserved.
doi:10.1016/j.ijheatmasstransfer.2006.03.008

Nomenclature

A_n	coefficient in the separation-of-variables solution for electric potential
b	dimensionless depth of the lower melt
B	magnetic flux density
c_p	specific heat of the melt
C	dimensionless concentration of the solute in the melt
C^*	concentration or mole fraction of solute in the melt
C_o	mole fraction of aluminum–antimonide of replenished fluid from the upper melt
C_s	dimensionless concentration in the crystal
D	diffusion coefficient for the solute in the molten semiconductor
g	gravitational acceleration
Gr	thermal Grashof number
Gr_C	compositional or solutal Grashof number
h	dimensionless length of the crystal
I	total electric current
J_0	Bessel function of the first kind and zeroth order
J_1	Bessel function of the first kind and first order
J_c	characteristic electric current density
$\mathbf{j}$	dimensionless electric current density
k	thermal conductivity of the melt
k_s	segregation coefficient for aluminum–antimonide in gallium–antimonide
n	summation index
N	interaction parameter
$\hat{\mathbf{n}}$	outward unit normal vector
p	dimensionless pressure
Pe_g	growth Péclet number
Pe_m	species transport Péclet number
Pr	Prandtl number
r	dimensionless radial coordinate in the melt
r_o	radial position for estimation of the characteristic electric current density
$\hat{\mathbf{r}}$	unit vector in the radial direction for the cylindrical coordinate system
R	crystal's radius or outer electrode's inner radius
Re	Reynolds number
Re_m	magnetic Reynolds number
t	dimensionless time
T	dimensionless temperature in the melt
T^*	temperature in the melt
T_c	freezing temperature of pure gallium–antimonide
T_h	uniform and constant temperature of the submerged heater's surface
T_m^*	melting temperature
T_m	dimensionless melting temperature
U_c	characteristic velocity of the melt
U_g	growth rate or velocity of the crystal–melt interface
$\mathbf{v}$	dimensionless velocity in the melt
v_r	dimensionless radial velocity in the melt
v_θ	dimensionless azimuthal velocity in the melt
v_z	dimensionless axial velocity in the melt
z	dimensionless axial coordinate in the melt
$\hat{\mathbf{z}}$	unit vector in the axial direction for the cylindrical coordinate system

Greek symbols

$(\Delta C)_o$	characteristic mole fraction variation
$(\Delta T)_o$	difference between the heater's surface temperature and the melting temperature of pure gallium–antimonide
α	dimensionless growth rate or velocity of the crystal–melt interface
β_C	compositional coefficient of volumetric expansion
β_T	thermal coefficient of volumetric expansion
ϕ	dimensionless electric potential
Φ_o	dimensionless uniform and constant electric potential of the center electrode
γ_e	dimensionless radius of the center electrode
γ_h	dimensionless radius of the submerged fused-silica heater housing
Γ	difference between the solute concentration at the periphery and at the centerline for the crystal which solidified after steady-state transport has been achieved
κ_1	constant in velocity profile for the axial gap flow
κ_2	constant in velocity profile for the axial gap flow
λ_n	eigenvalues of the Bessel function of the first kind and zeroth order
Λ	buoyancy ratio
μ	dynamic viscosity of the melt
μ_p	magnetic permeability of the melt
π	3.14159 radians
θ	dimensionless azimuthal coordinate in the melt
$\hat{\theta}$	unit vector in the azimuthal direction for the cylindrical coordinate system
ρ	density of the melt
ρ_o	density of the melt at the melting temperature
σ	electrical conductivity of the melt
ψ	dimensionless Stokes streamfunction in the melt
ζ	dimensionless rescaled axial coordinate in the melt

melt with a composition that offsets the rejection of species along the crystal–melt interface [5,6]. Since the rejection of gallium–antimonide along the solidification front leaves the melt more rich in GaSb, the lower melt is continuously replenished with material from the upper melt which has the alloy composition that is desired for the grown crystal.

Ostrogorsky and Müller [7] have shown that this modified bottom-seeded VGF method produces crystals which exhibit much lower defect densities and much more compositional uniformity than crystals grown by the LEC process. Ma et al. [8] and Wang et al. [9] demonstrated that this VGF method using submerged heater growth is an extremely promising method for producing doped crystals with axially uniform composition and relatively good radial homogeneity.

Since molten gallium–antimonide and aluminum–antimonide are good electrical conductors, a radial electric current in the melt can be used together with an axial magnetic field in order to electromagnetically stir the melt and control the species distribution in the semiconductor crystal, which depends on the convective and diffusive transport of the species in the melt. In the laboratory, we have demonstrated that a radial electric current in the presence of a steady axial magnetic field can produce a significant stirring rate in a gallium–antimonide melt which has a 50 mm diameter and 1 cm depth [10]. Some of the advantages of electromagnetic (EM) stirring for bottom-seeded crystal growth are enhancement of the radial compositional uniformity, reduction of thermal stresses, minimization of defect densities, and the ability to grow at faster rates. The large number of adjustable crystal growth parameters and the larger number of ways to combine them make process optimization through empirical trial-and-error extremely tedious. Therefore, models that predict the distribution of alloy components in the melt are very useful for optimizing the complex growth process.

In a previous investigation [8], we modelled the effects of applying weak magnetic and electric fields on the dopant transport during the VGF process using submerged heater growth. We provided predictions of the steady-state three-dimensional axisymmetric melt motion due to thermally driven buoyant convection and electromagnetic stirring and then coupled transient species transport of a dopant for the entire period of time needed to grow a crystal. We found that both the radial and axial compositional homogeneity in the doped crystal improved as the strength of the electromagnetic (EM) stirring increased. Holmes et al. [11] found that rotation of the heater further improves this homogeneity. For the growth of alloyed crystals, such as gallium–aluminum–antimonide (GaAlSb), the crystal is solidified from a solution of gallium–antimonide (GaSb) and aluminum–antimonide (AlSb) in which the concentration of the solute is not small. Gallium–antimonide has a density of 6030 kg/m^3 while aluminum–antimonide has a density of 4720 kg/m^3, so that the heavier gallium–antimonide sinks while the lighter aluminum–antimonide rises. This density difference drives an additional flow, i.e., compositionally driven buoyant convection, or solutal convection. In the present paper, we present a numerical model for the coupled unsteady equations governing the melt motion and the transport of aluminum–antimonide in a gallium–antimonide solution for this process.

2. Problem formulation

This paper treats the unsteady, axisymmetric transport of aluminum–antimonide in a gallium–aluminum–antimonide melt during the vertical gradient freeze crystal growth using a submerged heater with an externally applied, uniform, steady, axial magnetic field $B\hat{\mathbf{z}}$ combined with a radial electric current. Here, B is the magnetic flux density, while $\hat{\mathbf{r}}$, $\hat{\theta}$ and $\hat{\mathbf{z}}$ are the unit vectors for the cylindrical coordinate system. Our dimensionless problem is sketched in Fig. 1. The coordinates and lengths are normalized by the outer electrode's inner (or center) radius R, which is equal to the crystal radius, so that γ_e is the dimensionless radius of the center electrode, γ_h is the dimensionless radius of the submerged fused-silica heater housing, and b is the dimensionless depth of the lower melt. A single crystal seed, which initiates solidification, lies at the bottom of the fused-silica crucible. A graphite disc and a boron nitride disc lie below the crucible. These discs are cooled by a water-cooled hearth which removes heat along the bottom of the crucible. As the crystal at $z = \alpha t$ solidifies, the crystal–melt interface moves axially upward at the dimensionless rate $\alpha = U_g/U_c$, where U_g is the constant growth rate and U_c is the characteristic velocity of the melt while z is normalized by the crystal's radius R and t is time normalized by R/U_c. The lower melt is replenished with liquid supplied from the upper melt through a small annular gap between the submerged heater housing and the outer electrode. The submerged heater at $z = \alpha t + b$ moves upward at the same rate so that the depth of the melt is constant throughout growth. A long small-diameter cylindrical

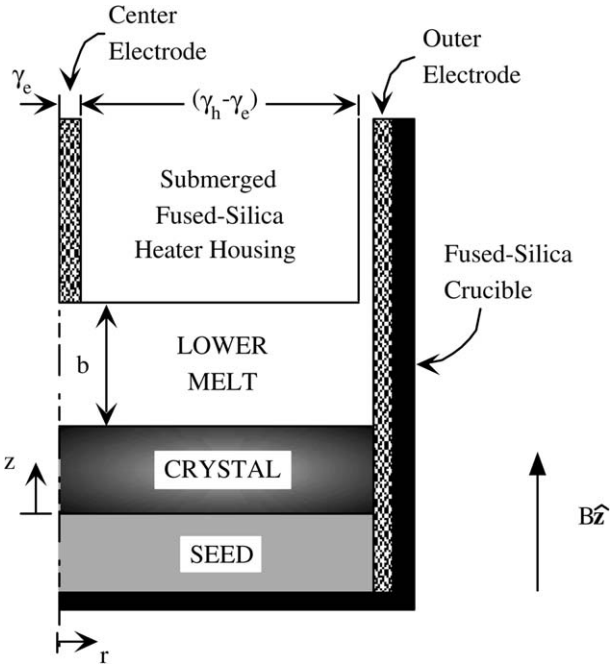

Fig. 1. VGF process using submerged heater growth with a uniform, steady, axial magnetic field $\hat{\mathbf{z}}$ and with a steady radial electric current where coordinates are normalized by the crystal's radius.

graphite electrode through the center of the submerged heater carries a constant axially downward DC electric current. The electrical conductivity of the graphite electrodes is far larger than that of the fused-silica submerged heater housing and also larger than that of the solid alloy crystal.

A magnetic field is applied with a copper coil outside the heater insulation, while an electric current is applied through the electrode so that the electromagnetic (EM) body force created by this electric current is balanced by the inertial force. This balance gives a characteristic velocity

$$U_c = \left(\frac{BJ_cR}{\rho_o}\right)^{1/2}, \tag{1}$$

where R is the inner radius of the outer electrode or the radius of the crystal, and ρ_o is the density of the molten semiconductor at the melting temperature T_m. Here, the characteristic electric current density is $J_c = I/(2\pi r_o bR)$, where r_o is a radial position that we use to provide an approximate estimate of the radial electric current density, and I is the externally applied radial electric current. For example, for a crystal grown with $R = 25$ mm, $bR = 1$ mm and $I = 4$ A, our estimation of J_c is 6366.2 A/m^2 with $r_o = 1$ cm.

The electric current in the melt produces an induced magnetic field which is superimposed upon the applied magnetic field produced by the external magnet. The characteristic ratio of the induced to applied magnetic field strengths is the magnetic Reynolds number, $Re_m = \mu_p\sigma U_cR$, where μ_p is the magnetic permeability of the melt and σ is the electrical conductivity of the melt. For all crystal growth processes, $Re_m \ll 1$ and the additional magnetic fields produced by the electric currents in the melt are negligible.

Ohm's law is

$$\mathbf{j} = -\nabla\phi + N\mathbf{v}\times\hat{\mathbf{z}}, \tag{2}$$

where $\mathbf{j}$ is the electric current density normalized by J_c, ϕ is the electric potential normalized by J_cR/σ, and $\mathbf{v} = v_r\hat{\mathbf{r}} + v_\theta\hat{\boldsymbol{\theta}} + v_z\hat{\mathbf{z}}$ is the melt velocity normalized by U_c. Here, the ratio of the induced electric field $\mathbf{v}\times\hat{\mathbf{z}}$ to the static electric field $\nabla\phi$ is the interaction parameter, $N = \sigma B^2R/\rho_oU_c$. For the present process, $N = 5.78\times10^{-7}$ so that the induced electric field is negligible. Wang et al. [12] modelled the transport for non-zero values of N. For our axisymmetric problem, there is no azimuthal flow of electric current, and the electric potential is governed by

$$\nabla^2\phi = 0. \tag{3}$$

We treat the electrodes as perfect conductors which carry a uniform electric potential, so that the boundary conditions are

$$\phi = 0, \quad \text{at } r = 1 \text{ for } -1 \leqslant \zeta \leqslant +1, \tag{4a}$$

$$\phi = \Phi_o, \quad \text{at } \zeta = +1 \text{ for } 0 \leqslant r \leqslant \gamma_e. \tag{4b}$$

Here, $\zeta = -1 + 2(z - \alpha t)/b$ is a rescaled axial coordinate so that $-1 \leqslant \zeta \leqslant +1$. The fused-silica heater, the annular gap between the heater and the outer electrode, and the crystal–melt interface are treated as electrical insulators, so that $\hat{\mathbf{n}}\cdot\nabla\phi = 0$ along each of these boundaries, where $\hat{\mathbf{n}}$ is the outward unit normal vector.

The electric potential is given by a separation-of-variables solution,

$$\phi = \sum_{n=1}^{\infty} A_n\Phi_oJ_o(\lambda_nr)\frac{\cosh\left[\frac{\lambda_nb}{2}(\zeta+1)\right]}{\cosh(\lambda_nb)}, \tag{5}$$

where J_o is the Bessel function of the first kind and zeroth order and λ_n are the eigenvalues of J_o. Based on our choice for the characteristic electric current density J_c, the integral of the radial electric current over the melt depth must equal b at $r = r_o$, so that

$$\Phi_o = b\left[\sum_{n=1}^{\infty} A_nJ_1(\lambda_nr_o)\frac{\sinh(\lambda_nb)}{\cosh(\lambda_nb)}\right]^{-1}, \tag{6}$$

where J_1 is the Bessel function of the first kind and first order. A Galerkin method is implemented to avoid a Gibb's phenomena associated with the discontinuous boundary conditions along $\zeta = +1$. The electric current originates from the center electrode and flows radially outward and axially downward. For $\gamma_e = 0.1905$ and $b = 0.4$, $\Phi_o = 1.353$.

We assume that the temperature differences and compositional variations are sufficiently small so that all of the thermophysical properties of the melt can be considered uniform and constant except for the density in the gravitational body force term of the Navier–Stokes equation. In this Boussinesq approximation, the characteristic temperature difference $(\Delta T)_o = (T_h - T_c)$ and characteristic mole fraction difference $(\Delta C)_o$ are assumed to be sufficiently small that melt's density is a linear function of temperature and concentration, given by

$$\rho = \rho_o[1 - \beta_T(T^* - T_c) - \beta_C(C^* - C_o)], \tag{7}$$

and that $\beta_T(\Delta T)_o \ll 1$ and $\beta_C(\Delta C)_o \ll 1$ where β_T and β_C are the thermal and the compositional coefficients of volumetric expansion, respectively. In Eq. (7), T^* is the temperature in the melt, T_c is the freezing temperature of pure gallium–antimonide, C^* is the mole fraction of aluminum–antimonide in the melt, and C_o is the constant mole fraction of aluminum–antimonide in the upper melt which is continuously fed to the lower melt through the gap at $\zeta = +1$.

The equations governing the axisymmetric melt velocity, temperature, and mole fraction are

$$\frac{\partial\mathbf{v}}{\partial t} + (\mathbf{v}\cdot\nabla)\mathbf{v} = -\nabla p + \frac{1}{Re^2}[GrT + Gr_C(C-1)]\hat{\mathbf{z}} + \frac{\partial\phi}{\partial r}\hat{\boldsymbol{\theta}} + \frac{1}{Re}\nabla^2\mathbf{v}, \tag{8a}$$

$$\nabla\cdot\mathbf{v} = 0, \tag{8b}$$

$$PrRe\left[\frac{\partial T}{\partial t} + (\mathbf{v}\cdot\nabla)T\right] = \nabla^2T + \chi j^2, \tag{8c}$$

$$Pe_m\left[\frac{\partial C}{\partial t}+(\mathbf{v}\cdot\nabla)C\right]=\nabla^2 C, \tag{8d}$$

$$v_r=\frac{1}{r}\frac{\partial\psi}{\partial z}, \tag{8e}$$

$$v_z=-\frac{1}{r}\frac{\partial\psi}{\partial r}, \tag{8f}$$

where p is the deviation of the dimensional pressure from the hydrostatic pressure for a uniform density normalized by $\rho_o U_c^2$, T is the deviation of the dimensional temperature from the melting temperature of pure gallium–antimonide, $T_c = 710$ °C, normalized by $(\Delta T)_o$, and C is the mole fraction of aluminum–antimonide in the melt normalized by C_o. In Eq. (8a), the ratio of the thermal buoyancy force to the electromagnetic (EM) body force is Gr/Re^2, where $Gr=\rho_o^2 g\beta_T(T_h-T_c)R^3/\mu^2$ is the thermal Grashof number and $Re=\rho_o U_c R/\mu$ is the Reynolds number. Here, $g=9.81$ m^2/s and μ is the dynamic viscosity of the melt. The solutal or compositional Grashof number $Gr_C=\rho_o^2 g\beta_C C_o R^3/\mu^2$ is equal to ΛGr with $\Lambda=\beta_C C_o/\beta_T(\Delta T)_o$, which was used by Farrell and Ma [1] and referred to as the buoyancy ratio by Bennacer and Gobin [13]. In Eq. (8c), the Prandtl number is $Pr=\mu c_p/k$, where c_p and k are the specific heat and thermal conductivity of the melt, respectively. In Eq. (8c), the characteristic ratio of Joule heating to conductive heat transfer is $\chi=R^2J_c^2/[\sigma_k(T_h-T_m)]$. For the present process, $\chi=7.4\times 10^{-5}$ so that Joule heating is negligible. In Eq. (8d), the species transport Péclet number is $Pe_m=U_c R/D$, where D is the diffusion coefficient for aluminum–antimonide in the melt. In Eqs. (8e) and (8f), we introduce a Stokes streamfunction ψ for the radial and axial velocities for the meridional melt motion which identically satisfies continuity (8b) for our axisymmetric melt motion.

We use a reference frame moving with the fused-silica heater and crystal–melt interface. Therefore, the no-slip and no-penetration conditions on the surface of the outer electrode are

$$v_r=v_\theta=0,\quad \text{at } r=1 \text{ for } -1\leqslant\zeta\leqslant+1, \tag{9a, b}$$

$$v_z=-\alpha,\quad \text{at } r=1 \text{ for } -1\leqslant\zeta\leqslant+1. \tag{9c}$$

The boundary conditions on the crystal–melt interface and on the surfaces of the center electrode and fused-silica heater are

$$v_r=v_\theta=0,\quad \text{at } \zeta=-1 \text{ for } 0\leqslant r\leqslant 1, \tag{10a, b}$$

$$v_z=-\alpha,\quad \text{at } \zeta=-1 \text{ for } 0\leqslant r\leqslant 1, \tag{10c}$$

$$v_r=v_\theta=0,\quad \text{at } \zeta=+1 \text{ for } 0\leqslant r\leqslant 1, \tag{10d, e}$$

$$v_z=0,\quad \text{at } \zeta=+1 \text{ for } 0\leqslant r\leqslant \gamma_h. \tag{10f}$$

Assuming that the density of the crystal and melt are the same, the gap between the heater and the outer electrode replenishes the solidifying melt at a volumetric flowrate $\pi\alpha$, so that we assume a simple velocity profile [8],

$$v_z=\alpha[-1+\kappa_1(1-r)+\kappa_2(1-r^2)],\quad \text{at } \zeta=+1 \text{ for } \gamma_h\leqslant r\leqslant 1, \tag{11}$$

where $\kappa_1=3(1+\gamma_h^2)/(1-\gamma_h)^3$ and $\kappa_2=-2(1+\gamma_h+\gamma_h^2)/(1-\gamma_h)^3(1+\gamma_h)$.

The power provided by the submerged heater above the lower melt and the heaters to the periphery of the crucible is adjusted so that the crystal–melt interface is nearly planar, and the melt adjacent to the submerged heater is held at a uniform and constant temperature T_h. Therefore, we apply the thermal conditions

$$T=1,\quad \text{at } \zeta=+1 \text{ for } 0\leqslant r\leqslant 1, \tag{12a}$$

$$\frac{\partial T}{\partial r}=0,\quad \text{at } r=1 \text{ for } -1\leqslant\zeta\leqslant+1. \tag{12b}$$

Along the crystal–melt interface,

$$T=T_m,\quad \text{at } \zeta=-1 \text{ for } 0\leqslant r\leqslant 1, \tag{13}$$

where T_m is the deviation of the dimensional melting temperature T_m^* from T_c normalized by (T_h-T_c). Here,

$$T_m^*(C^*)=710+855C^*-1111C^{*2}+1060C^{*3}-450C^{*4}, \tag{14}$$

where T_m^* is in °C. Eq. (14) is an estimation of the melting temperature as a function of mole fraction of aluminum–antimonide C^* which is based upon the experimental data for the liquidus curve in the pseudo-binary phase diagram for gallium–aluminum–antimonide [14].

The segregation coefficient $k_s(C^*)$ for aluminum–antimonide (AlSb) in gallium–antimonide (GaSb) is greater than unity, so that the gallium–antimonide is rejected along the crystal–melt interface producing a GaSb-rich region adjacent to the crystal–melt interface. A curve fit based on the experimental data presented by Osamura et al. [14] gives a relationship

$$k_s(C^*)=7.3-53.9C^*+253.7C^{*2}-672.3C^{*3}+979.45C^{*4}-727.88C^{*5}+214.7C^{*6}. \tag{15}$$

Before solidification begins, the melt contains initially pure gallium–antimonide, so that $C(r,\zeta,t=0)=0$. In order to compensate for the rejection of gallium–antimonide along the crystal–melt interface, the lower melt is replenished with liquid having mole fraction C_o, so that the boundary condition along the gap between the heater and the outer electrode is

$$C=1,\quad \text{at } \zeta=+1 \text{ for } \gamma_h\leqslant r\leqslant 1. \tag{16}$$

The boundary condition along the crystal–melt interface is

$$\frac{2}{b}\frac{\partial C}{\partial\zeta}=Pe_g(k_s-1)C,\quad \text{at } \zeta=-1 \text{ for } 0\leqslant r\leqslant 1, \tag{17}$$

where $Pe_g=U_g R/D=\alpha Pe_m$ is the growth Péclet number. The conditions along the impermeable surfaces of the center electrode, outer electrode and fused-silica heater are $\hat{\mathbf{n}}\cdot\nabla\mathbf{C}=0$.

We use a Chebyshev spectral collocation method with a second-order implicit time integration scheme to solve Eqs. (8a)–(8d) with Gauss–Lobatto collocation points in r and ζ. We use a sufficient number of collocation points in order

to resolve velocity, temperature and concentration gradients near the boundaries. We integrate from $t = 0$ to a t which is slightly less than h/α, where h is the dimensionless length of the crystal. We use a large enough number of time steps such that the results do not change by increasing the number of time steps. The calculations were performed on the Cray X1 and IBM pSeries 690. For $C_o = 0.005$, we used 96 collocation points in the radial direction, 31 collocation points in the axial direction, and 16,000 time steps, and the simulation took 12 min to complete one time step. When we increased the number of collocation points in radial direction to 201, the maximum value of the streamfunction changed by 0.06% and the maximum value of the concentration changed by 0.019% at $t = 0.1665$. When we increased the number of collocation points in axial direction to 61, the maximum value of streamfunction changed by 0.0001% and the maximum value of the concentration changed by 0.0001% at $t = 0.1665$. When we increased the number of time steps to 24,000, the maximum value of streamfunction changed by 0.9% and the maximum value of the concentration changed by 0.0002% at $t = 0.1665$.

Assuming that the species do not diffuse in the solid crystal and that the density of the solid and liquid are the same, the mole fraction of aluminum–antimonide normalized by C_o in the crystal $C_s(r,z)$ is given by $C_s(r,z) = k_s C(r, \zeta = -1, t = z/\alpha)$. Future research will compare model predictions to experimental measurements for the concentration in the crystal.

3. Results

We present results for $\gamma_e = 0.1905$, $\gamma_h = 0.8$, $h = 3.2$, $Pr = 0.0442$, $b = 0.4$, and $U_g = 2$ mm/h for which $Pe_g = 0.6944$ and $Gr = 2 \times 10^6$ with $(T_h - T_c) = 20$ K. We investigate the effects of increasing the value of C_o on the transport in the melt and the alloy segregation in the crystal. The parameters as a function of U_c and C_o are $Re = 6.526 \times 10^4 U_c$, $Pe_m = 1.25 \times 10^6 U_c$, $Gr_C = 2.269 \times 10^8 C_o$, $\alpha = 5.556 \times 10^{-7} U_c^{-1}$, and the dimensionless time to grow a crystal is $h/\alpha = 5.76 \times 10^6 U_c$, where U_c is in m/s.

The purpose of the present study is to investigate the effects of increasing the initial concentration C_o on the transport in the melt and on the compositional distribution in the crystal. We present results for $Re = 30$, for which $U_c = 0.0004597$ m/s, $Pe_m = 574.63$, $\alpha = 0.0012085$, and $h/\alpha = 2647.9$. The only remaining parameter is Gr_C, which is a function of C_o.

We begin by presenting results for doped growth in which the concentration of the dopant or solute is so small that the melt is considered dilute. For doped growth, we assume that the concentrations differences are not large enough to drive solutal convection so that the melt motion is independent of the dopant transport and steady [8]. Thus the melt motion is governed by Eqs. (8a)–(8c) with $Gr_C = 0$ and without the time derivatives. We solve Eq. (8d) for the dopant concentration in the melt with v_r and v_z given by the solution to Eqs. (8a)–(8c). We present contours for the temperature T, the azimuthal velocity v_θ, and the meridional streamfunction ψ, in Fig. 2a–c, respectively, for $Re = 30$. In Fig. 2a, the isotherms are horizontal so that there is no radial temperature gradient and no thermally driven buoyant convection. The electromagnetic (EM) stirring provides an azimuthal body force which drives an azimuthal melt motion presented in Fig. 2b, where the minimum value of v_θ is -0.5170. The meridional melt motion in Fig. 2c is dominated by the motion of the heater and the replenished flow, so that the melt adjacent to the periphery of the ampoule flows axially downward and then either solidifies or flows radially inward along the crystal–melt interface. Viscous shearing causes this flow to drive a clockwise circulation adjacent to the centerline. The minimum and maximum values of the meridional streamfunction are $\psi_{min} = -0.0003089$ and $\psi_{max} = 0.0006044$, respectively. In Fig. 3a and b, we present the constant-concentration curves for the concentration in the melt at $t = 6.6196$ and at $t = 357.46$, respectively. The concentration of the replenished fluid is $C = 1$ along the gap for $\gamma_h \leqslant r \leqslant 1$ at $\zeta = +1$ for all time, as reflected in Fig. 3a.

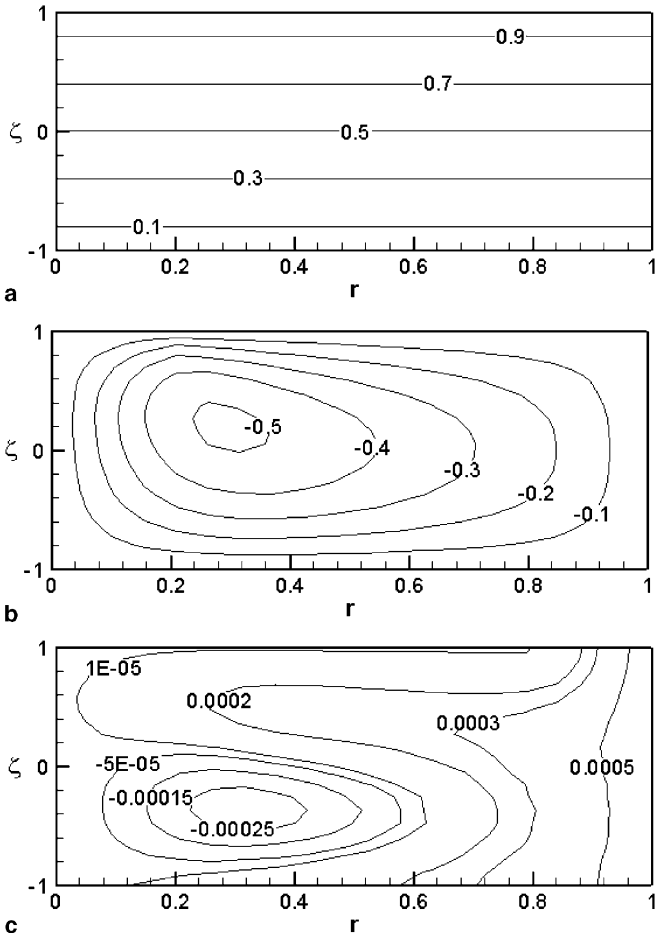

Fig. 2. Contours for the steady-state melt motion for doped growth for $Re = 30$: (a) temperature $T(r,\zeta)$, (b) azimuthal velocity $v_\theta(r,\zeta)$, (c) meridional streamfunction $\psi(r,\zeta)$.

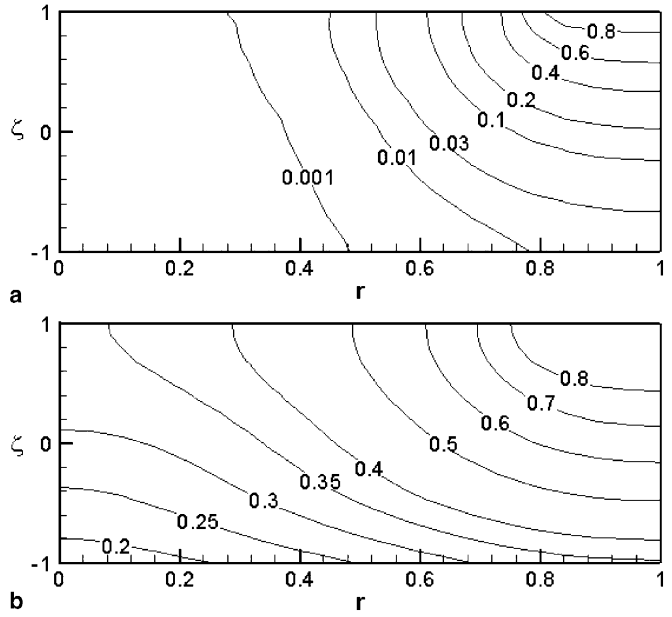

Fig. 3. Constant-concentration curves for doped growth for $Re = 30$ in the melt $C(r,\zeta,t)$: (a) $C(r,\zeta,t = 6.6197)$, (b) $C(r,\zeta,t = 357.46)$.

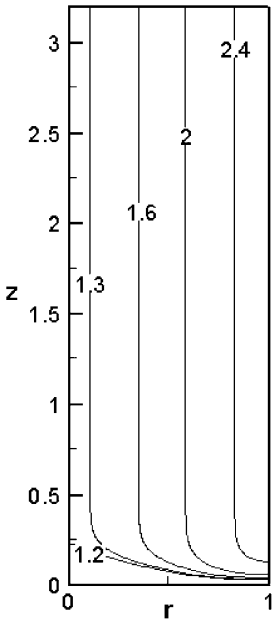

Fig. 4. Constant-concentration curves in the crystal $C_s(r,z)$ for doped growth and $Re = 30$.

The crystal absorbs aluminum–antimonide during solidification because $k_s > 1$ so that the concentration is $C < 1$ in a significant fraction of the melt. The melt adjacent to the centerline at $r = 0$ remains at $C = 0$ for this early stage of growth. At $t = 357.46$ when 13.5% of the crystal has grown, the dopant transport has reached a steady state. The constant-concentration curves at this time are presented in Fig. 3b in which the minimum value of the concentration is $C = 0.1713$. After this time, the dopant distribution in the melt remains the same as shown in Fig. 3b so that the remainder of the crystal solidifies with the same radial distribution. The constant-concentration curves in the crystal are presented in Fig. 4. The bottom of the crystal, which solidified before the dopant transport reached steady state, reflects an axial variation in C_s. The remainder of the crystal which solidified after steady-state dopant transport has been achieved is axially uniform with the same radial distribution. This corresponds to the top 86.5% of the crystal. We define the difference between the solute concentration at the periphery and at the center for the crystal which solidified after steady-state transport has been achieved, $\Gamma = C_s(1, 3.199) - C_s(0, 3.199)$. For the doped crystal, this difference is $\Gamma = C_s(1, 3.199) - C_s(0, 3.199) = 1.24475$.

We present results for $C_o = 0.000005$ for which $Gr_C = 1.13 \times 10^3$. At early stages of growth, the meridional melt motion resembles Fig. 2c except for a small counterclockwise circulation near $r = 1$. The concentration differences in the melt are large enough to drive compositionally driven or solutal convection, which is reflected in the meridional melt motion. We present contours of the meridional streamfunction ψ and the concentration C after steady-state transport has been achieved in the melt at $t = 321.1$ when 12.125% of the crystal has grown in Fig. 5a and b,

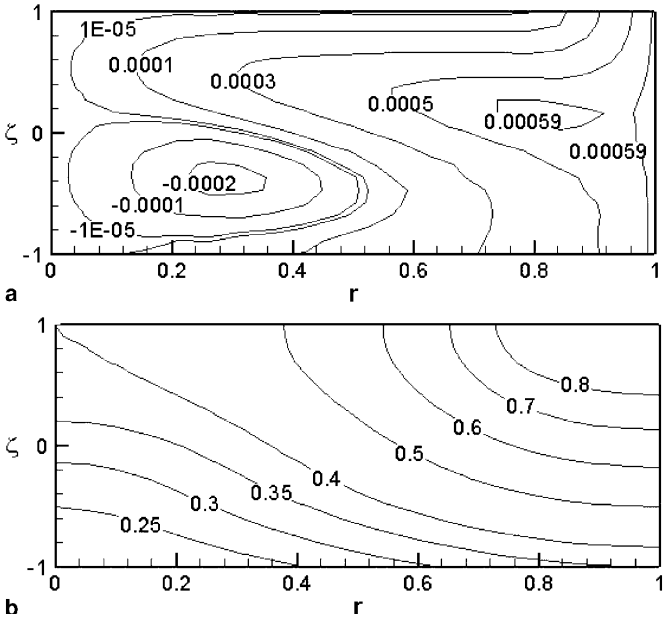

Fig. 5. Contours in the melt for $Re = 30$ and $C_o = 0.000005$ at $t = 321.1$: (a) meridional streamfunction $\psi(r,\zeta,t = 321.1)$, (b) melt concentration $C(r,\zeta,t = 321.1)$.

respectively. At this time, the azimuthal velocity v_θ nearly resembles the contours in Fig. 2b for doped growth but the minimum value of v_θ has increased to -0.5137. In Fig. 5a, the minimum and maximum values of the meridional streamfunction are -0.0002348 and 0.0006058, respectively. The constant-concentration curves in Fig. 5b show that the concentration of the solute, aluminum–antimonide, near $r = 1$ is larger than the concentration near the centerline at a given axial position. Because AlSb is lighter

than GaSb, the solutal convection alone would drive a meridional circulation in the counterclockwise direction. This explains the small counterclockwise circulation near the periphery in Fig. 5a, and explains the increase in the magnitude of the meridional streamfunction compared with doped growth in which there is no solutal convection. The counterclockwise solutal convection cancels some of the clockwise circulation adjacent to the centerline in Fig. 5a. The counterclockwise flow due to solutal convection augments the radially inward flow due to the replenishment in the gap. This causes the melt having higher solute concentration to convect towards the centerline along the interface having lower solute concentration at a faster rate compared with doped growth. This has the effect of decreasing the concentration difference along the interface compared with doped growth for the equivalent stage of growth, as reflected in Fig. 5b. In Fig. 5b, the minimum value of the solute concentration is 0.1828. The addition of solutal convection increases the mixing of the melt so that the transport in the melt reaches a steady state at an earlier stage of growth compared with doped growth. The constant-concentration curves for the solute concentration in the crystal are presented in Fig. 6. After the transport in the melt has reached a steady state, the remainder of the crystal solidifies with the same radial solute distribution. Therefore the bottom 12.125% of the crystal has an axial variation and the top 87.875% of the crystal is axially uniform. The difference between the solute concentration at the periphery and at the centerline for the crystal that has solidified after steady-state transport has been achieved is $\Gamma = 1.22947$.

We present results for $C_o = 0.005$ for which $Gr_C = 1.13 \times 10^6$. With this elevated level of the replenished solute concentration C_o, the solutal convection is much stronger compared with $C_o = 0.00005$. This increased mixing in the melt causes the melt motion and solute transport to reach a steady state at an earlier time $t = 289.6$ when 10.9375% of the crystal has grown. At this time, the azimuthal velocity v_θ nearly resembles the contours in Fig. 2b for doped growth but the minimum value of v_θ has further increased to -0.4923. We present the contours of the meridional streamfunction ψ and the solute concentration C in the melt at $t = 289.6$ in Fig. 7a and b, respectively. The solutal convection has significantly increased the counterclockwise circulation in Fig. 7a, as reflected by the $\psi = 0.001$ and $\psi = 0.003$ contours. In Fig. 7a, the minimum and maximum values of the meridional streamfunction are -0.0002029 and 0.004162, respectively. The solutal convection has dramatically decreased the radial segregation as reflected in Fig. 7b in which most of the constant-concentration curves are nearly horizontal. In Fig. 7b, the minimum value of the solute concentration is 0.3496. The top 89.0625% of the crystal solidifies is axially uniform with the same radial distribution, as shown in Fig. 8. The difference between the solute concentration at the periphery and at the centerline for the crystal that has solidified after steady-state transport has been achieved is $\Gamma = 0.01608$.

In Fig. 9, we present the radial distribution of the solute concentration for the crystal which solidified after steady-state transport has been reached for $C_o = 0.00025$, $C_o = 0.001$ and $C_o = 0.005$. As the concentration of the replenished flow through the gap C_o increases, the radial segregation decreases as reflected in the decreasing value of Γ. For doped growth corresponding to $C_o = 0$, $\Gamma =$

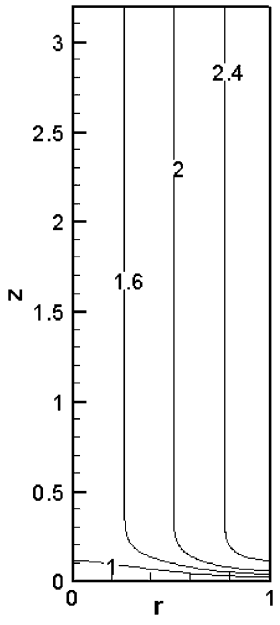

Fig. 6. Constant-concentration curves in the crystal $C_s(r,z)$ for $Re = 30$ and $C_o = 0.000005$.

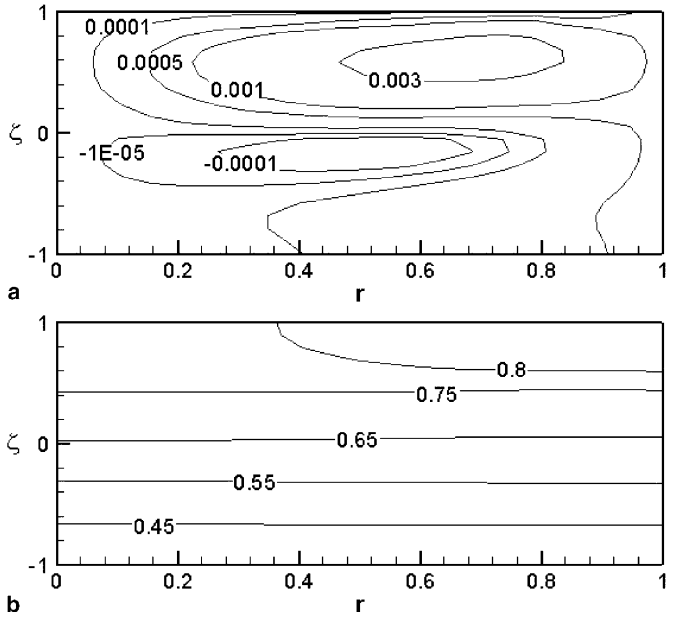

Fig. 7. Contours in the melt for $Re = 30$ and $C_o = 0.005$ at $t = 289.6$: (a) meridional streamfunction $\psi(r,\zeta,t = 289.6)$, (b) melt concentration $C(r,\zeta,t = 289.6)$.

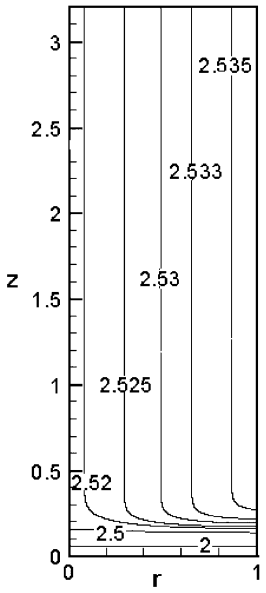

Fig. 8. Constant-concentration curves in the crystal $C_s(r,z)$ for $Re = 30$ and $C_o = 0.005$.

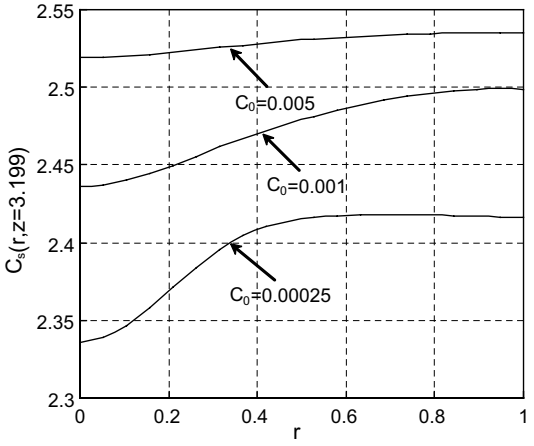

Fig. 9. Radial segregation in the crystal $C_s(r, z = 3.199)$ after steady-state transport has been reached for $C_o = 0.00025$, $C_o = 0.001$ and $C_o = 0.005$.

1.24475. Γ decreases as C_o increases. That is, $\Gamma = 1.22947$ for $C_o = 5 \times 10^{-6}$, $\Gamma = 0.08030$ for $C_o = 0.00025$, $\Gamma = 0.06245$ for $C_o = 0.001$, and $\Gamma = 0.01608$ for $C_o = 0.005$. The radial and axial segregation in the crystal is summarized in Table 1 for different values of C_o.

Table 1
Radial and axial segregation after steady-state transport has been reached

C_o	Γ	Percentage of crystal which is axially uniform (%)
0	1.24475	86.50
0.000005	1.22947	87.25
0.00025	0.0803	87.50
0.001	0.06245	88.62
0.005	0.01608	89.06

4. Conclusions

We developed a numerical model for the unsteady transport during the VGF process by submerged heater growth with a steady axial magnetic field and a steady radial electric current. We investigated the effects of solute concentration on the melt motion and species transport in the melt and on the solute distribution in the crystal. As the solute concentration in the melt increases, the solutal convection in the melt becomes stronger which decreases the concentration difference in the melt. Consequently, the radial segregation in the crystal decreases as the solutal convection increases. Additionally, the increased mixing due to solutal convection decreases the time that it takes for the transport in the melt to reach steady state and increases the length of the crystal that solidifies with axial uniformity.

Acknowledgments

This research was supported by the US Air Force Office of Scientific Research under grant FA9550-04-1-0249. The calculations were performed on the Cray X1 provided by the DoD High Performance Computing Modernization Program under grant AFSNH2487 and on the IBM pSeries 690 provided by the National Computational Science Alliance under grant DMR030015.

References

[1] M.V. Farrell, N. Ma, Macrosegregation during alloyed semiconductor crystal growth in strong axial and transverse magnetic fields, Int. J. Heat Mass Transfer 47 (2004) 3047–3055.
[2] J.L. Morton, N. Ma, D.F. Bliss, G.G. Bryant, Dopant segregation during liquid-encapsulated Czochralski crystal growth in a steady axial magnetic field, J. Cryst. Growth 242 (2002) 471–485.
[3] Y. Ohmori, K. Sugii, S. Akai, K. Matsumoto, LEC growth of Te-doped GaSb single crystals with uniform carrier concentration distribution, J. Cryst. Growth 60 (1982) 79–85.
[4] A.G. Ostrogorsky, Numerical simulation of single crystal growth by submerged heater method, J. Cryst. Growth 104 (1990) 233–238.
[5] N. Ma, J.S. Walker, A model of dopant transport during Bridgman crystal growth with magnetically damped buoyant convection, J. Heat Transfer 122 (2000) 159–164.
[6] J.M. Hirtz, N. Ma, Dopant transport during semiconductor crystal growth axial versus transverse magnetic fields, J. Cryst. Growth 210 (2000) 554–572.
[7] A.G. Ostrogorsky, G. Müller, Normal and zone solidification using the submerged heater method, J. Cryst. Growth 137 (1994) 64–71.
[8] N. Ma, D.F. Bliss, G.W. Iseler, Vertical gradient freezing of doped gallium–antimonide semiconductor crystals using submerged heater growth and electromagnetic stirring, J. Cryst. Growth 259 (2003) 26–35.
[9] X. Wang, N. Ma, D.F. Bliss, G.W. Iseler, P. Becla, Comparing modified vertical gradient freezing with rotating magnetic fields or with steady magnetic and electric fields, J. Cryst. Growth 287 (2006) 270–274.
[10] X. Wang, N. Ma, D.F. Bliss, G.W. Iseler, Semiconductor crystal growth by modified vertical gradient freezing with electromagnetic stirring, J. Thermophys. Heat Transfer 19 (2005) 95–100.
[11] A.M. Holmes, X. Wang, N. Ma, D.F. Bliss, G.W. Iseler, Vertical gradient freezing using submerged heater growth with rotation and

with weak magnetic and electric fields, Int. J. Heat Fluid Flow 26 (2005) 792–800.

[12] X. Wang, N. Ma, D.F. Bliss, G.W. Iseler, A numerical investigation of dopant segregation by modified vertical gradient freezing with moderate magnetic and weak electric fields, Int. J. Eng. Sci. 43 (2005) 908–924.

[13] R. Bennacer, D. Gobin, Cooperating thermosolutal convection in enclosures—I. Scale analysis and mass transfer, Int. J. Heat Mass Transfer 39 (1996) 2671–2681.

[14] K. Osamura, K. Nakajima, Y. Murakami, Experimental and calculation of the Al–Ga–Sb ternary phase diagram, J. Electrochem. Soc. 126 (1979) 1992–1997.